

# Multifunctional 3D Patternable Drug-Embedded Nanocarrier-Based Interfaces to Enhance Signal Recording and Reduce Neuron Degeneration in Neural Implantation

Wei-Chen Huang, Hsin-Yi Lai, Li-Wei Kuo, Chia-Hsin Liao, Po-Hsieh Chang, Ta-Chung Liu, San-Yuan Chen,\* and You-Yin Chen\*

Over the past two decades, prosthetic devices have been successfully applied to treat neurodegenerative disease.<sup>[1]</sup> However, the long-term utilization is limited by adverse biological reactions in host tissues, resulting in signal failure of the implanted devices.<sup>[2]</sup> The ability to mimic tissue with the mechanical and structural properties of neural implanted devices is critical for reducing the inevitable tissue responses.<sup>[3–5]</sup> Although the development of flexible polymer-based implants with polyimide and Parylene C has significantly alleviated initial mechanical injury, the mechanical stress ( $\approx 1$  GPa) is still quite mismatched to brain tissue properties ( $\approx 100$  kPa).<sup>[6]</sup> Given this challenge, numerous studies have utilized various conductive polymer (CP) composites or conductive hydrogels, including CP-alginate,<sup>[7]</sup> PEDOT (poly(3,4-ethylenedioxythiophene))-PAA (polyacrylic acid),<sup>[8]</sup> CP-pHEMA (poly(2-hydroxyethyl methacrylate)),<sup>[9]</sup> and (PEDOT)/poly(vinyl alcohol)-heparin,<sup>[10]</sup> as the coating to improve the electrochemical performance and biocompatibility of neural electrodes.<sup>[10,11]</sup> For example, Poole-Warren and co-workers explored the incorporation of multiple functional biological molecules such as sericin and gelatin into conductive hydrogels to promote neural cell adhesion and proliferation.<sup>[10,11]</sup> Martin and Abidian reported the use of CP

nanotubes on the chronic neural microelectrode to improve the neuronal spike recordings of metal electrode sites.<sup>[7,12]</sup> In addition, they further demonstrated that the release of an anti-inflammatory drug (dexamethasone) can be precisely controlled from the CP nanotubes by external electrical stimulation.<sup>[13]</sup> However, it is more important to design biocompatible coatings for the implanted devices to mimic mechanical and structural properties of brain tissues in order to reduce inevitable tissue responses for long-term utilization. Therefore, 3D nanostructural coatings should be developed for the insulated regions, rather than the electrode sites of neural implants, so that the whole implant body can more stably interface with the nearby brain tissues.<sup>[3,14]</sup> Although the nanomaterial-based substrate coatings incorporated into drug delivery systems such as poly(lactic-co-glycolic acid) (PLGA) nanoparticles,<sup>[15]</sup> pHEMA,<sup>[16]</sup> or PLGA nanoparticles-embedded matrix have been developed, these systems lack stable physical and chemical properties for reducing tissue responses, including an appropriate nanostructural interface, mechanical properties, and biofouling ability.<sup>[2,17,27]</sup> Multifunctional drug-embedded coatings must be developed and integrated into the nanostructural neural interfaces to allow sustained release of bioactive molecules (anti-inflammatory drugs) and simultaneous construction of a brain tissue-mimic but bioinert microenvironment for reducing both acute and chronic inflammation reactions during long-term implantation.<sup>[3,7,14]</sup> In this work, we aimed to develop a neuronal interface with the following functional capabilities: (1) structural and mechanical properties mimicking brain tissue, (2) sustained nonfouling property to inhibit tissue encapsulation, and (3) prolonged anti-inflammatory ability to reduce tissue responses. With the integration of nanomanufacturing technology and multifunctional nanomaterials into the neural implants, we can extensively reduce the reactive tissue responses, provide continuous protection of surviving neurons, and ensure long-term performance reliability of implants.

Therefore, we proposed the novel combination of antioxidative zwitterionic nanocarriers and nanomanufacturing technology to develop a new 3D nanocarrier-based neural interface that support long-term neural implantation and achieve better therapy for chronic diseases. The schematic diagram in **Figure 1a** demonstrates our experimental procedure. A new type of anti-inflammatory nanogel was developed based on the amphiphilic polydimethylsiloxane-modified N, O-carboxylic chitosan (PMSC) incorporated with oligo-proanthocyanidin (OPC) (named OPMSC) (Note 1, Supporting Information). The natural OPC can be used as an anti-inflammatory drug due to

Dr. W.-C. Huang, Dr. P.-H. Chang, Dr. T.-C. Liu,  
Prof. S.-Y. Chen  
Department of Materials Science and Engineering  
National Chiao Tung University  
No. 1001, Ta-Hsueh Rd., Hsinchu 30010, Taiwan  
E-mail: sanyuanchen@mail.nctu.edu.tw

Prof. H.-Y. Lai  
Interdisciplinary Institute of  
Neuroscience and Technology  
Qiushi Academy for Advanced Studies  
Zhejiang University  
No. 268, Kaixuan Road, Hangzhou City  
Zhejiang Province 310029, China

Dr. L.-W. Kuo  
Institute of Biomedical Engineering and Nanomedicine  
National Health Research Institutes  
No. Keyan Road, Miaoli 35053, Taiwan

Dr. C.-H. Liao  
Department of Medical Research  
Buddhist Tzu Chi General Hospital  
No. 707, Sec. 3, Chung-Yang Rd., Hualien 97002, Taiwan

Prof. Y.-Y. Chen  
Department of Biomedical Engineering  
National Yang Ming University  
No. 155, Sec. 2, Linong St., Taipei 11221, Taiwan  
E-mail: irradiance@so-net.net.tw

DOI: 10.1002/adma.201500136



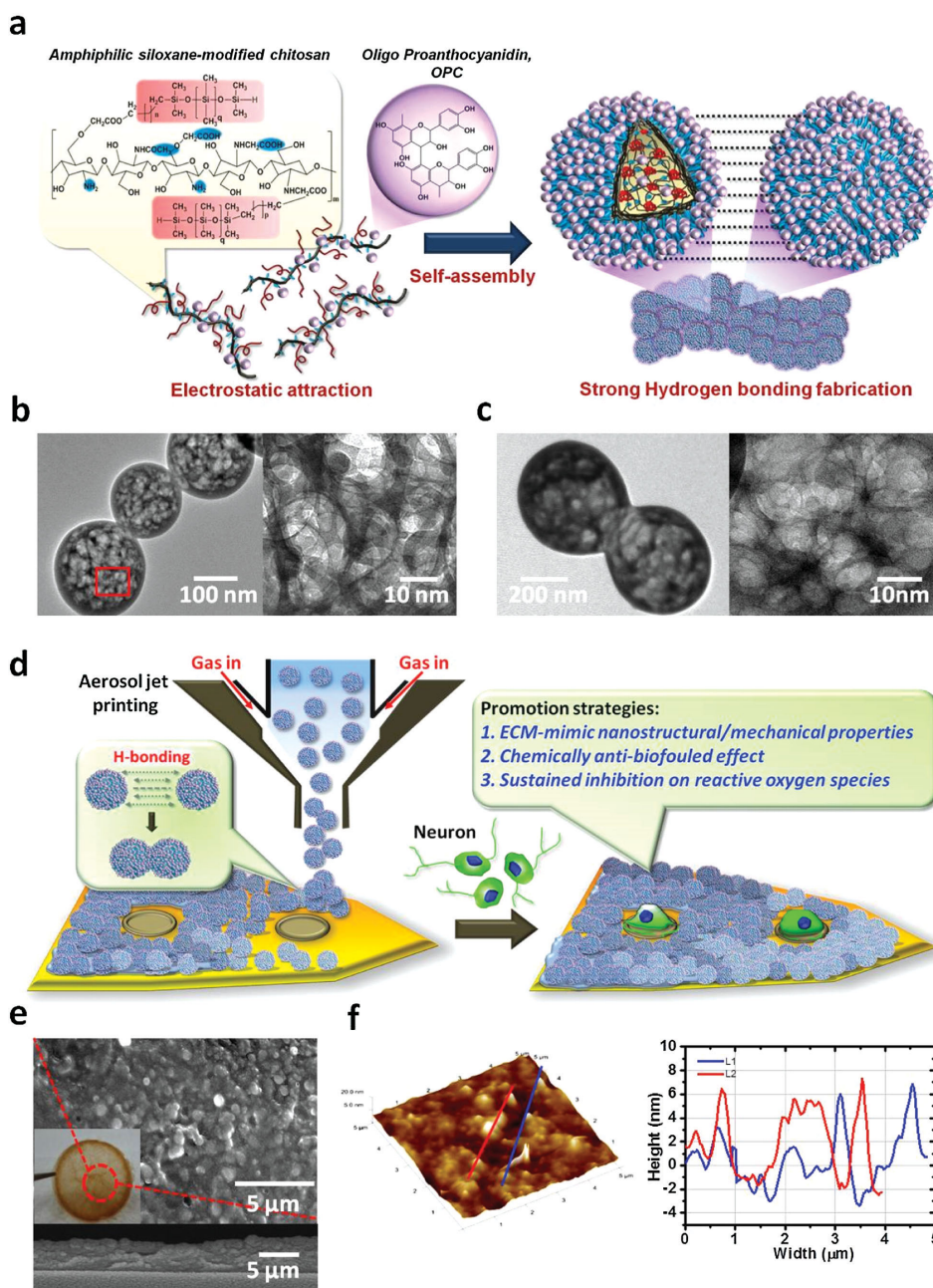


**Figure 1.** a) Schematic illustration of the mechanism for formation of nanogel-based membrane based on the self-assembly of OPC-incorporated amphiphilic polydimethylsiloxane-modified N, O-carboxylic chitosan (OPMSC), followed by hydrogen-bonding interaction of OPC. The TEM images display the network structure of b) PMSC and c) OPMSC spherical nanogels. d) Using aerosol jet printing, the OPMSC suspensions were directly patterned on a neural probe to create an anti-inflammatory neural interface. The top and cross-section views of SEM images in e) provide evidence that the OPMSC nanogels can self-assemble together into a membrane structure following aerosol jet printing. f) Topographical view obtained by AFM analysis shows the nanoscaled roughness of the OPMSC hydrogel.

its multipotent therapeutic effects on neurodegenerative diseases.<sup>[18]</sup> Furthermore, given the abundance of hydroxyl groups and the aromatic architecture, the semi-hydrophilic OPC can act as a structural stabilizer to help the self-adhesion of nanogels, making the structure evolve into a biostable 3D anti-inflammatory neural interface.<sup>[19–21]</sup> As shown in Figure 1b, PMSC self-assembled into spherical network nanostructures about 150–200 nm in size, where the inner intertextures

composed of hydrophobic and hydrophilic nanodomains demonstrated both biomimic structures and large surface areas.<sup>[22]</sup> The exposure of hydrophilic functional groups (carboxylic groups and amino groups) resulted in hydrogen bonding, which enabled slight adhesion between the freestanding nanogels. As the OPMSC incorporated 20% OPC, it also displayed a spherical network structure, but the size was larger than that of the PMSC (Figure 1c). More importantly, the enhancement of

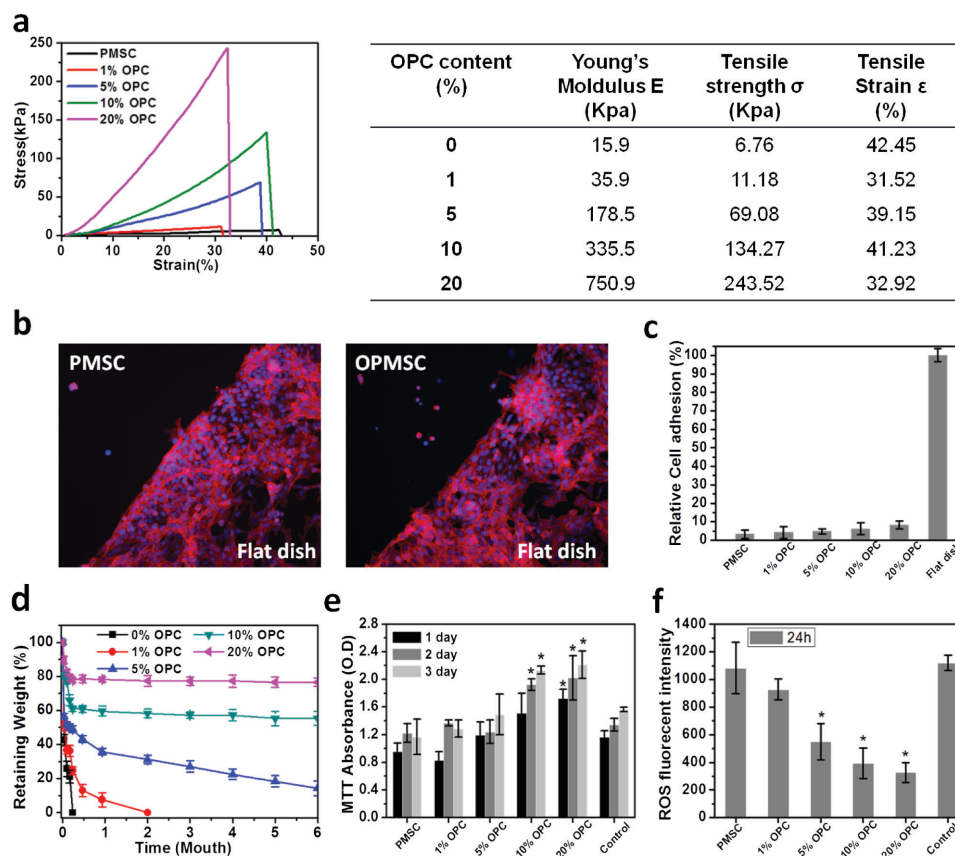


**Figure 2.** a) The mechanical properties of OPMSC hydrogel incorporating 0%, 1%, 5%, 10%, and 20% OPC obtained by strain–stress measurement to demonstrate the rubber elasticity. b) Representative fluorescence microscopy images (10 $\times$  magnification) demonstrated that the CTXT-NA2 cells preferred attaching to the flat dish rather than PMSC and OPMSC (scale bar equals 100  $\mu$ m). c) Relative cell adhesion ratios of the OPMSC membranes incorporated with different OPC ratios. Data are expressed as means  $\pm$  S.D. d) The retaining weight of OPMSC with 0%, 1%, 5%, 10%, and 20% OPC incorporation after six-month in vitro enzymatic degradation. e) Cell viability of PC12 cells after one-day, two-day, and three-day incubation with the OPMSC suspensions. The OPMSC with 10 and 20 wt% OPC shows the enhancement on cell proliferation. f) The ROS production by PC12 cells after 24 h incubation with the OPMSC suspensions. The lower fluorescent intensity of OPMSC demonstrates the inhibitory effect of OPC on the generation of intracellular ROS, which decreased with more OPC incorporation ( $^*P < 0.05$  when compared with control).

hydration interactions provided by OPC helped to connect the nanogels more closely.

Next, we directly fabricated OPMSC nanogels onto a membrane by aerosol jet printing technology because it is a low-temperature and noncontact process that allows direct printing of the OPC-incorporated PMSC nanogels onto the functional 3D interface of the microscaled patterned polyimide-based neural probe without any thermal or acidic damage to the anti-oxidant activity of OPC (in Figure 1d).<sup>[23]</sup> The process involved atomizing the OPMSC nanogels into a mist, and then focusing them out of the jet head by gas flow. The operating parameters, i.e., focusing ratio (FR), which is the gas flow rate, offer an additive driving force to help pile up the OPMSC nanogels more densely and tightly (Note 2, Supporting Information). As illustrated in Figure S1 of the Supporting Information, when FR was less than 4, the printed feature displayed freestanding spherical nanogels in morphology. However, when FR was increased up to 4, the nanogels tended to adhere to each other because more water molecules were carried along with the OPMSC to provide the hydration ability. When FR was larger than 5, the printed OPMSC could be directly constructed to

form a 3D nanocarrier-based membrane (Figure 1e). Further confirmed by Fourier Transform Infrared Spectroscopy (FTIR) analysis in Supporting Information, Figure S2 of Note 3, the architecture was indeed constructed by the hydrogen-bonding interaction between –OH groups of OPC and –NH<sub>2</sub> groups of PMSC, as indicated in the broad band for O–H stretching at 3400 nm<sup>-1</sup>, the shift for the amide bending at 1550 nm<sup>-1</sup>, as well as the broad band for the out-of-plane N–H wagging of amide at 650 nm<sup>-1</sup>. Atomic Force Microscopy (AFM) analysis in Figure 1f shows that the OPMSC surface has topography with a nanoscaled roughness in the range of 4–10 nm, which provides more stable contact with the brain tissues.<sup>[24]</sup>

As we know, the mechanical properties are the primary concern in the development of neural implants.<sup>[3]</sup> Thus, the tensile test was performed to obtain the stress–strain curves of OPMSC gel membrane with different ratios of OPC incorporation. As illustrated in Figure 2a, all the curves correlate with the rubber elasticity theory, demonstrating Gaussian extending behaviors.<sup>[25]</sup> We found that the OPC incorporation led to an increase in modulus E (15.9 kPa), tensile strength  $\sigma$  (6.76 kPa), and tensile strain  $\epsilon$  (42.45%) up to 40–50 times due to the

strong hydrogen-bonding interaction between OPC and PMSC. The Scanning Electron Microscope (SEM) images in Figure S3 of the Supporting Information demonstrate that the OPC incorporation resulted in an increased crosslink density and made the porous structure denser compared to PMSC gel membrane (very soft and ductile), which provides strong evidence that the incorporated OPC not only strengthened the structure of the PMSC, but also increased the elastic modulus to hundreds of kPa, which was well matched to the properties of brain tissue.

To reduce nonspecific bio-interactions and prevent subsequent inflammatory responses including leukocyte activation, tissue fibrosis, thrombosis coagulation, and additional infection,<sup>[26]</sup> we further measured the cell-substrate interactions using OPMSC gel membrane with different OPC concentrations to investigate the adhesion ability of glia cells, i.e., astrocytes, for 24 h. In our system, PMSCs with both carboxyl groups and amino groups demonstrated zwitterionic properties to allow a higher hydration ability, which can produce better antifouling property.<sup>[27]</sup> As shown in the fluorescent images in Figure 2b, both PMSC and OPMSC membranes imparted the anti-adhesion ability to cells. Moreover, a linear relationship was found between the equilibrium water content (EWC) and OPC incorporation ratio (Figure S4, Supporting Information). The accession of OPC may deplete these ionized groups and in turn reduce the hydrophilicity, but the OPMSC with 20% OPC incorporation still displayed a much lower cell adhesion ratio (9.2%),<sup>[28]</sup> indicating that the OPMSC possessed a high antibi-fouling ability to inhibit the adhesion of glial cells.

To use the neural probe for chronic brain implantation, the biostability of the neural interface including the long-term anti-biodegradation and noncytotoxicity must be further evaluated. In Figure 2d, the *in vitro* biodegradation test showed that the PMSC gel membrane was completely hydrolyzed after six-day digestion, while OPMSC with 5%, 10%, and 20% OPC could maintain an intact structure with a retaining weight ratio of 14.5%, 55.4%, and 76.3%, respectively, until six months because OPC acts as a natural structure stabilizer of the OPMSC membrane.<sup>[19]</sup> To investigate the cytotoxicity of the degraded OPMSC debris, we explored cell viability by 3-(4,5-Dimethylthiazol-2-yl)-2,5-diphenyltetrazolium bromide (MTT) cell viability assay. After three-day incubation, PC12 cells in the medium supplemented with PMSC exhibited similar staining intensity compared to that of the control group, indicating no toxicity (Figure 2e). Comparably, OPMSC promoted cell proliferation, especially when the incorporated OPC concentration reached 10 and 20 wt%. To further elucidate the effect of OPMSC on cell proliferation, we measured the intracellular reactive oxygen species (ROS) levels by taking advantage of 2', 7'-Dichlorodihydrofluorescein diacetate (DCF-DA), which can permeate the cell membrane and form fluorescent products after interacting with peroxides generated by cells.<sup>[29]</sup> As shown in Figure 2f, OPMSC incorporated with more OPC resulted in reduced generation of intracellular ROS. The results demonstrated that the anti-oxidative polyphenols enabled suppression of the intercellular ROS, in turn enhancing the cell physiology.<sup>[21,29]</sup> Therefore, OPMSC again displayed a long-term anti-inflammatory effect.

In order to use the OPMSC in a microscaled neural implant, we assessed the stability of the cell-micropatterning by culturing neural cells on PMSC and OPMSC arrays with  $\approx 30 \mu\text{m}$  in width

and  $\approx 10 \mu\text{m}$  in thickness (Figure 3a). Figure 3b,c shows that the PC12 cells on both PMSC-coated and OPMSC-coated (20% OPC) substrates exhibited neurite sprouting and outgrowth up to  $40 \mu\text{m}$  after four-day incubation. However, only the cells on OPMSC-patterned substrates were successfully confined to exhibit the mono-axial extension of synapses along with the micropatterns. This means the OPMSC with OPC incorporation could prevent degradation by enzymes secreted from the cells, enabling long-term stability of cell-micropatterning.

Subsequently, we integrated OPMSC into the flexible polyimide-based microprobe (Note 5 and Figure S5, Supporting Information). Through aerosol jet printing, the OPMSC (with 20% OPC) could be directly printed on the insulate surfaces with the exposure of only Au electrodes (Figure 3d). Since the neural interface is typically subjected to destruction by tissue fluids with chronic use, maintaining the bonding stability is critical for use as a long-term biocompatible neural probe. After washing three to five times with deionized water, we analyzed the morphology to demonstrate the structural stability and integration of OPMSC membrane on the polyimide-based probe (see cross-section view in Figure 3e). We used FTIR analysis to investigate the chemical bonding interaction between the OPMSC-probe interfaces (Note 6, Supporting Information), and the spectra in Figure S6 of the Supporting Information show that the peaks at  $655$ ,  $807$ , and  $920 \text{ cm}^{-1}$ , which are attributed to C–H wagging vibration of the benzene ring, weakened and broadened. On the other hand, the peak at  $1055 \text{ cm}^{-1}$  disappeared due to symmetrical ether linkage of polyimide. The presence of the strong hydrogen bonding and  $\pi$ – $\pi$  stacking forces demonstrates the self-healing ability in the wet environment and stabilizes the interface between OPMSC and polyimide-based probe.<sup>[30]</sup> To further investigate the OPC release behavior of the interface, the OPC release profiles of the probes coated with PMSC and OPMSC (1% OPC and 20% OPC) at  $\text{pH} = 7.4$  were obtained using UV absorption (Note 7, Supporting Information). As shown in Figure 3f, the neural probe coated with OPMSC with 1% OPC resulted in a burst-like OPC release, resulting in 50% accumulated release after 2 d. However, the neural probe coated with OPMSC with 20% OPC resulted in a slower release rate, and showed only 15% accumulated release until 7 d. The release rate decreased with an increase in the OPC content, implying that the OPC release was related to the degradation of OPMSC (Figure 2d). Therefore, the OPC embedded in the OPMSC through hydrogen bonding interactions can achieve sustained release. To further prove the long-term biostability of the probes,<sup>[31]</sup> we investigated cell adhesion and differentiation over a seven-day period. The SEM images in Figure 3g show that no cells adhered to the OPMSC insulate surface of the neural probe, while the cells only adhered to Au microelectrodes with a spherical shape. The results indicate that the OPMSC-coated neural probe offers cell-repellent ability, ensuring that cells only contact the microelectrodes.

To assess the possibility for further application of neural prosthetics in pathological disorders requiring chronic neural implantation, we evaluated the *in vivo* electrode–tissue interface impedance and neural recording ability of the OPMSC-coated probe after implantation in the deep brain by investigating signal-to-noise ratios over time. To examine the stability

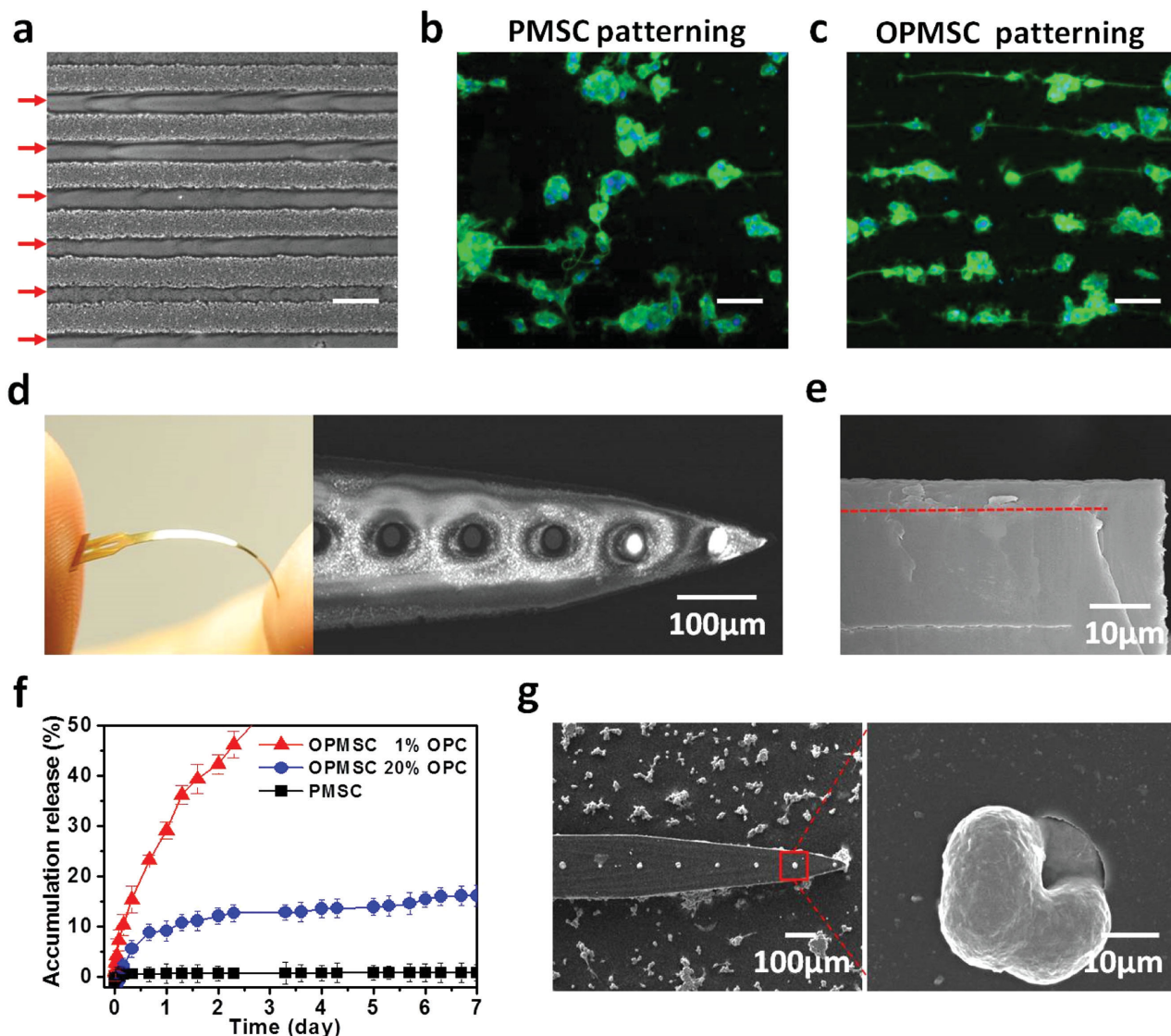


**Figure 3.** a) Optical microscopy (OM) image showing the patterning morphology of PMSC and OPMSC arrays with a thickness of  $\approx 30 \mu\text{m}$  obtained by aerosol jet printing (scale bar equals to  $100 \mu\text{m}$ ). The red arrows indicate the patterned location. Comparison of PC12 cell patterning on b) PMSC and c) OPMSC arrays demonstrates that OPMSC can maintain structural stability in the biological microenvironment (scale bar equals  $100 \mu\text{m}$ ). d) An overview and SEM images of the flexible OPMSC-coated polyimide (PI) probe (length =  $1.48 \text{ cm}$ ). e) SEM image showing a cross-sectional view of OPMSC-coated probe after washing with water. f) OPC release profiles of probes coated with PMSC and OPMSC at  $\text{pH} = 7.4$ . g) SEM images of PC12 cells growing on the OPMSC-coated neural probe. The enlarged view demonstrates that the PC12 cells only grow at the site of gold microelectrodes.

of evoked neuronal responses over time, we used a modified neural probe<sup>[32]</sup> with a single shank. Rats were implanted with a neural probe with thickness of  $50 \mu\text{m}$ , length of  $5 \text{ mm}$ , shank width of  $220 \mu\text{m}$ , and tip width of  $3 \mu\text{m}$  (Note 8, Supporting Information). Since the efficacy of implanted probes is mainly influenced by impedance, we measured the in vivo impedance of the implanted noncoated and OPMSC-coated neural probes over the lifetime (Notes 9 and 10, Supporting Information). We found that the OPMSC coating indeed reduced the impedance of the electrode–electrolyte interface compared to noncoated probes for all durations (Figure S7, Supporting Information). For further investigation, the neural signals were recorded in the ventroposteromedial/ventroposteriolateral (VPM/VPL)

thalamic nuclei of the rats (Note 11 and Figure S8, Supporting Information). Both signal-to-noise ratio (SNR) and the yield rate of multiple single-units of the noncoated and OPMSC-coated neural probes over the lifetime were subsequently measured and calculated at multiple time points (Figure 4a). As shown in Figure 4b (black solid line), on day 28 after implantation, the SNR in OPMSC-coated neural probe group ( $P$ -value  $< 0.05$ ;  $N = 5$ ) exhibited no significant decrease compared to that in the noncoated probe group ( $P$ -value  $< 0.05$ ;  $N = 5$ ), indicating that the OPMSC-coated neural probe produced stable chronic recordings. In addition, the mean yield rate of multiple single-units of OPMSC-coated neural probe ( $8 \pm 1.58$  unit yields) was significantly higher than that of the noncoated neural probe

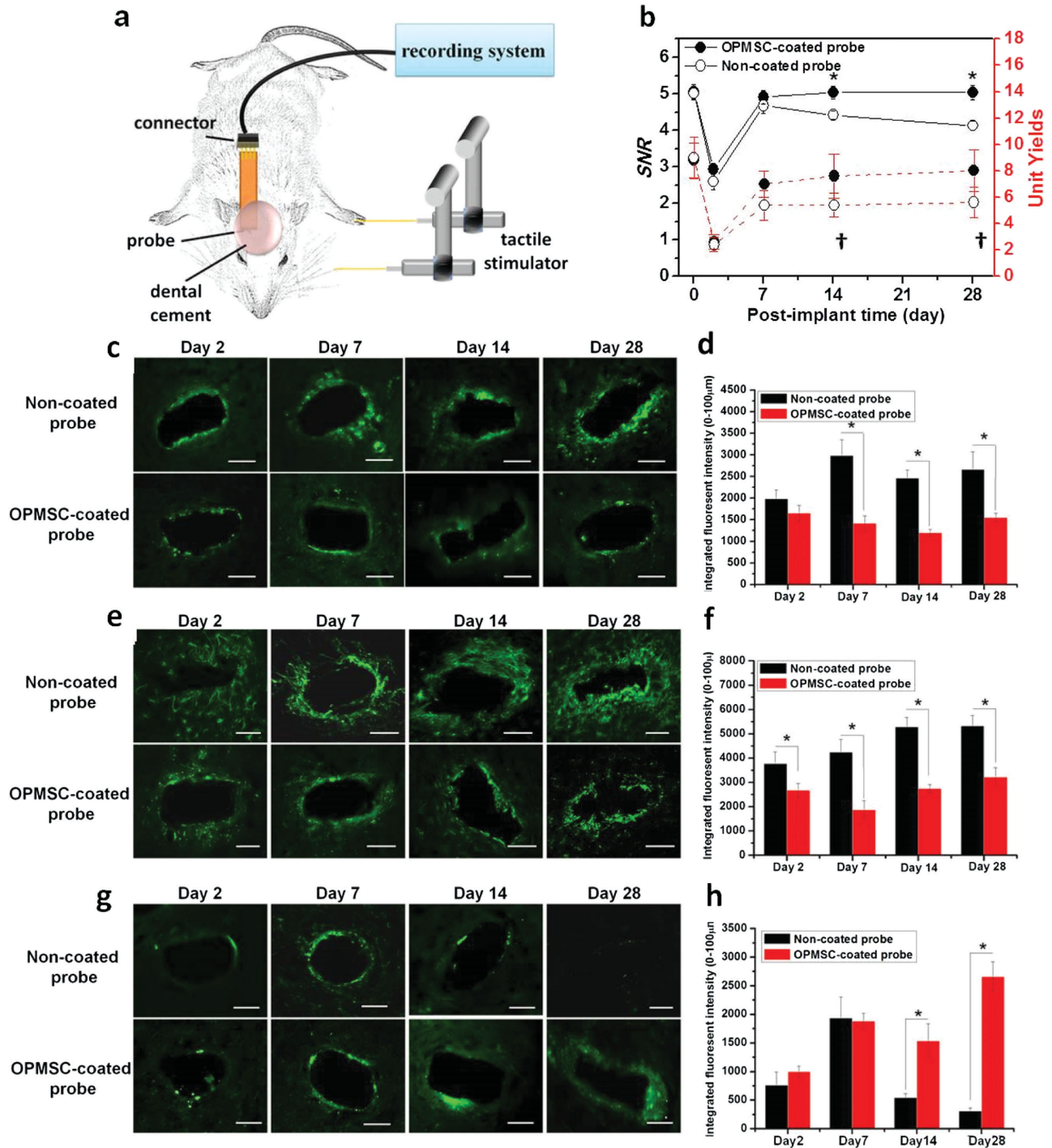


**Figure 4.** a) Experimental setup of the electrophysiological recording. b) Signal-to-noise ratio (SNR) and mean yield rate of multiple single-units versus time. Data are expressed as mean  $\pm$  S.D. (A) For SNR comparisons of neural recordings between the implanted OPMSC-coated and non-coated probes, significantly higher SNR recording was achieved with the implantation of OPMSC-coated probes at day 14 and day 28 compared to noncoated probe animals ( $N = 10$ ) on the same day ( $^*P < 0.05$ ). When comparing yield rate on microelectrodes from implanted OPMSC-coated and noncoated probes, the recording from a significantly large number of identified single units from the OPMSC-coated probe was favored at day 14 and day 28 in comparison to the yield rate of multiple units of the implanted noncoated probe animals ( $N = 10$ ) on the same day ( $^*P < 0.05$ ). c–h) Representative fluorescent images demonstrate tissue responses around the tip of the noncoated probe and the OPMSC-coated probe at days 2, 7, 14, and 28 post-implantation. (c) ED1 staining; (e) GFAP staining; (g) NeuN staining (scale bar equals 100  $\mu\text{m}$ ). Integral of fluorescent intensity 0–100  $\mu\text{m}$  from the microelectrode was obtained via the quantified expression of (d) ED1-staining, (f) GFAP-staining, and (h) NeuN-staining ( $^*P < 0.05$ , post hoc pairwise  $t$ -test).

( $5.6 \pm 1.14$  unit yields) by day 28 (red dotted line in Figure 4b). The results demonstrate that the probe coated with OPMSC is highly reliable for chronic recordings, which indeed improves the stability of long-term recordings.

To investigate and quantify the changes in tissue characteristics associated with the presence of a neural probe in brain tissue, we utilized diffusion tensor imaging (DTI) and derived the apparent diffusion coefficient (ADC), which represents the changes in water mobility in the vicinity of implanted brain tissue to character neuroinflammatory response<sup>[33]</sup> (Note 12, Supporting Information). Figure S11a, Supporting Information, shows a comparison of the ADC mappings at multiple time points between OPMSC-coated and noncoated probes. As shown in Figure S11b, Supporting Information, compared with noncoated probe, significantly lower ADC values were found at day 2 in the OPMSC-coated probe, indicating a lower increase in blood–brain barrier (BBB) permeability in response to the disruption of BBB.<sup>[34]</sup> From day 7 to day 28, relatively lower ADC values were found for the noncoated probe, implying that the lesion site was surrounded by a denser population of activated microglia, astrocytes, and dead neurons that reduce the water indwelling,<sup>[35]</sup> which are correlated to the increased microelectrode impedance at the implant surface.<sup>[17,36]</sup> A dense glial encapsulating layer around the probe will result in to higher noise<sup>[37]</sup> and lead to inconsistent recordings whereas the isolation of neurons leads to a low SNR.<sup>[38]</sup> Finally, to examine the effect of longitudinal pathological changes during neural probe implantation, we performed immunohistochemistry to assess staining for ED1, glial fibrillary acidic protein (GFAP), and neuronal nuclei (NeuN), which indicates activated microglia, astrocytes and neurons, respectively (Note 13, Supporting Information). The quantitative comparison of fluorescent intensity at 2, 7, 14, and 28 days after implantation was used to investigate the acute and chronic tissue responses (Figure 4c–h).<sup>[39]</sup> In Figure 4c, the ED1 expression was found within 50  $\mu\text{m}$  from the noncoated probe by day 2, and it gradually increased until day 28. Comparably, the ED1 expression was relatively lower in the vicinity of OPMSC-coated probe during the period. The quantified result in Figure 4d indicates that on day 28 after implantation, the ED1 expression of the noncoated probe was 1.5-fold higher than that of the OPMSC-coated probe. Similar results were also observed for GFAP expression. The GFAP expression of the tissues around the noncoated probe indicated that a large number of astrocytes were activated by day 2, and then they gradually migrated toward the probe to form a dense gliosis scar over 100  $\mu\text{m}$  away from the implanted site within 28 days (Figure 4e,f). In comparison, there was relatively lower GFAP expression in the vicinity of the OPMSC-coated neural probe. For day 28 implantation, the quantified GFAP expression of the noncoated neural probe showed that the intensity was two-fold higher than that of OPMSC-coated probe.

To our knowledge, the acute inflammation responses are mainly attributed to the mechanical lesion induced by the insertion of the implant into the surrounding tissues, which disrupts blood vessels and in turn, activates microglia and astrocytes during the implantation period.<sup>[5,39]</sup> Figure S14, Supporting Information, shows the comparison of tissue responses around the tip of the noncoated probe, PMSC-coated probe and

the OPMSC-coated probe at days 2 and 7 post-implantation. As shown in Figure S13, Supporting Information, the intensity of ED1 and GFAP expression with the PMSC-coated probe was weaker than that of the noncoated probe, but stronger than that of the OPMSC-coated probe on day 7 after implantation. The result indicates that as compared to the noncoated probe, the PMSC coating can provide a flexible/soft intermediate to reduce mechanical damage, so the tissue responses are reduced. Further, the addition of OPC could further alleviate inflammatory reactions by day 7 after implantation. Therefore, OPMSC demonstrates the synergistic effects of PMSC and OPC on reducing tissue responses. It is worth noting that for NeuN expression, there was no difference between the two groups on day 7 after implantation (Figure 4g,h), while by day 14 and day 28 after implantation, there was relatively higher NeuN expression around the OPMSC-coated probe. The results imply that the suppression of acute immune reactions reduces chronic tissues responses and enhances neuronal survival. In addition, according to our *in vitro* test demonstrating that the OPC efficiently reduced ROS generation in PC12 cells, the higher neuronal survival found by day 14 and day 28 after implantation of OPMSC-coated probe may be attributed to the OPC incorporation. As we know, extracellular ROS are directly neurotoxic, while intracellular ROS enhance the production of pro-inflammatory cytokines including tumor necrotizing factor (TNF- $\alpha$ ) and monocyte chemoattractant protein-1 (MCP-1) in microglia, which impacts chronic implantation.<sup>[40]</sup> Our study indicates the OPMSC-coated probe constructs a long-lasting anti-inflammatory environment to protect surrounding neurons for both acute and chronic implantation, and in turn improves the biostability for long-term recordings.

In summary, we developed a new type of antibiofouled/anti-inflammatory OPMSC nanocarrier and utilized aerosol jet printing technology to directly construct a patterned neural interface for chronic neural implantation. The 3D nanocarrier-based membrane composed of amphiphilic silicone-modified chitosan (PMSC) and natural antioxidant OPC agent mimicked brain tissue physical properties and demonstrated antibiofouling ability. After short-term and long-term *in vivo* implantation, the OPMSC-coated neural probe displayed a relatively lower impedance value and much higher signal stability compared to noncoated probe. The ADC obtained by magnetic resonance imaging (MRI) demonstrated that the OPMSC-coated probe alleviated edema at the acute phase, and further reduced tissue trauma in the chronic phase. Immunostaining of anti-NeuN, anti-ED1, and anti-GFAP around the implanted site further demonstrated that the OPMSC-coated probe significantly reduced the population of activated microglia and astrocytes for all durations, resulting in increased survival 28 d after implantation. Such multifunctional nanostructured OPMSC-coated neural probes can provide a long-lasting functional neural interface for long-term neural implantation.

## Supporting Information

Supporting Information is available from the Wiley Online Library or from the author.

## Acknowledgements

H.-Y.L., L.-W.K., and C.-H.L. contributed equally to this work. This work was financially supported by the National Science Council of the Republic of China, Taiwan under Contract of NSC 102-2221-E-009-024-MY3. The authors also thank 7T animal MRI Core Lab of the Neurobiology and Cognitive Science Center for technical and facility support and C. H. Hsieh and J. H. Chen of the Instrumentation Center for MRI experiments at National Taiwan University.

Received: January 10, 2015

Revised: May 12, 2015

Published online: June 13, 2015

- [1] a) S. F. Cogan, *Annu. Rev. Biomed. Eng.* **2008**, *10*, 275; b) J. F. Kerrigan, B. Litt, R. S. Fisher, S. Cranston, J. A. French, D. E. Blum, M. Dichter, A. Shetter, G. Baltuch, J. Jaggi, S. Krone, M. Brodie, M. Rise, N. Graves, *Epilepsia* **2004**, *45*, 346; c) A. B. Schwartz, *Annu. Rev. Neurosci.* **2004**, *27*, 487.
- [2] a) G. C. McConnell, H. D. Rees, A. I. Levey, C. A. Gutekunst, R. E. Gross, R. V. Bellamkonda, *J. Neural Eng.* **2009**, *6*; b) D. H. Szarowski, M. D. Andersen, S. Retterer, A. J. Spence, M. Isaacson, H. G. Craighead, J. N. Turner, W. Shain, *Brain Res.* **2003**, *983*, 23.
- [3] N. A. Kotov, J. O. Winter, I. P. Clements, E. Jan, B. P. Timko, S. Campidelli, S. Pathak, A. Mazzatenta, C. M. Lieber, M. Prato, R. V. Bellamkonda, G. A. Silva, N. W. S. Kam, F. Patolsky, L. Ballerini, *Adv. Mater.* **2009**, *21*, 3970.
- [4] a) T. D. Y. Kozai, N. B. Langhals, P. R. Patel, X. P. Deng, H. N. Zhang, K. L. Smith, J. Lahann, N. A. Kotov, D. R. Kipke, *Nat. Mater.* **2012**, *11*, 1065; b) L. Rao, H. H. Zhou, T. Li, C. Y. Li, Y. W. Y. Duan, *Acta Biomater.* **2012**, *8*, 2233; c) S. S. Rao, N. Han, J. O. Winter, *J. Biomater. Sci., Polym. Ed.* **2011**, *22*, 611; d) M. Ochoa, P. H. Wei, A. J. Wolley, K. J. Otto, B. Ziaie, *Biomed. Microdevices* **2013**, *15*, 437; e) R. W. Griffith, D. R. Humphrey, *Neurosci. Lett.* **2006**, *406*, 81.
- [5] G. Lind, C. E. Linsmeier, J. Schouenborg, *Sci. Rep.* **2013**, *3*.
- [6] a) T. Ware, D. Simon, R. L. Rennaker, W. Voit, *Polym. Rev.* **2013**, *53*, 108; b) T. Ware, D. Simon, D. E. Arreaga-Salas, J. Reeder, R. Rennaker, E. W. Keefer, W. Voit, *Adv. Funct. Mater.* **2012**, *22*, 3470; c) K. Lee, A. Singh, J. P. He, S. Massia, B. Kim, G. Raupp, *Sens. Actuators, B* **2004**, *102*, 67; d) B. D. Winslow, M. B. Christensen, W. K. Yang, F. Solzbacher, P. A. Tresco, *Biomaterials* **2010**, *31*, 9163.
- [7] M. R. Abidian, D. C. Martin, *Adv. Funct. Mater.* **2009**, *19*, 573.
- [8] T. Y. Dai, X. T. Qing, Y. Lu, Y. Y. Xia, *Polymer* **2009**, *50*, 5236.
- [9] G. Justin, A. Guiseppi-Elie, *Biomacromolecules* **2009**, *10*, 2539.
- [10] G. L. M. Cheong, K. S. Lim, A. Jakubowicz, P. J. Martens, L. A. Poole-Warren, R. A. Green, *Acta Biomater.* **2014**, *10*, 1216.
- [11] a) R. A. Green, R. T. Hassarati, L. Bouchinet, C. S. Lee, G. L. M. Cheong, J. F. Yu, C. W. Dodds, G. J. Suaning, L. A. Poole-Warren, N. H. Lovell, *Biomaterials* **2012**, *33*, 5875; b) R. A. Green, P. B. Matteucci, R. T. Hassarati, B. Giraud, C. W. D. Dodds, S. Chen, P. J. Byrnes-Preston, G. J. Suaning, L. A. Poole-Warren, N. H. Lovell, *J. Neural Eng.* **2013**, *10*.
- [12] M. R. Abidian, D. C. Martin, *Biomaterials* **2008**, *29*, 1273.
- [13] M. R. Abidian, D. H. Kim, D. C. Martin, *Adv. Mater.* **2006**, *18*, 405.
- [14] J. R. Capadona, K. Shanmuganathan, D. J. Tyler, S. J. Rowan, C. Weder, *Science* **2008**, *319*, 1370.
- [15] a) D. H. Kim, D. C. Martin, *Biomaterials* **2006**, *27*, 3031; b) C. T. Lo, P. R. Van Tassel, W. M. Saltzman, *Biomaterials* **2010**, *31*, 3631.
- [16] S. J. Jhaveri, M. R. Hynd, N. Dowell-Mesfin, J. N. Turner, W. Shain, C. K. Ober, *Biomacromolecules* **2009**, *10*, 174.
- [17] V. S. Polikov, P. A. Tresco, W. M. Reichert, *J. Neurosci. Methods* **2005**, *148*, 1.
- [18] a) K. S. Bhullar, H. P. V. Rupasinghe, *Oxidative Med. Cellular Longevity* **2013**; b) D. Bagchi, M. Bagchi, S. J. Stohs, D. K. Das, S. D. Ray, C. A. Kuszynski, S. S. Joshi, H. G. Pruess, *Toxicology* **2000**, *148*, 187.
- [19] B. Han, J. Jaurequi, B. W. Tang, M. E. Nimni, *J. Biomed. Mater. Res., Part A* **2003**, *65A*, 118.
- [20] B. S. Liu, *J. Biomed. Mater. Res., Part A* **2008**, *87A*, 1092.
- [21] W. Y. Zhai, J. Chang, K. L. Lin, J. Y. Wang, Q. Zhao, X. N. Sun, *Biomaterials* **2006**, *27*, 3684.
- [22] W. C. Huang, S. Y. Chen, D. M. Liu, *Soft Matter* **2012**, *8*, 10868.
- [23] a) A. Mahajan, C. D. Frisbie, L. F. Francis, *ACS Appl. Mater. Interfaces* **2013**, *5*, 4856; b) S. H. Kim, K. Hong, K. H. Lee, C. D. Frisbie, *ACS Appl. Mater. Interfaces* **2013**, *5*, 6580.
- [24] V. Brunetti, G. Maiorano, L. Rizzello, B. Sorce, S. Sabella, R. Cingolani, P. P. Pompa, *Proc. Natl. Acad. Sci. U.S.A.* **2010**, *107*, 6264.
- [25] L. X. Xiao, C. Liu, J. H. Zhu, D. J. Pochan, X. Q. Jia, *Soft Matter* **2010**, *6*, 5293.
- [26] a) S. Krishnan, C. J. Weinman, C. K. Ober, *J. Mater. Chem.* **2008**, *18*, 3405; b) S. F. Chen, L. Y. Li, C. Zhao, J. Zheng, *Polymer* **2010**, *51*, 5283; c) Q. A. Yu, Y. X. Zhang, H. W. Wang, J. Brash, H. Chen, *Acta Biomater.* **2011**, *7*, 1550.
- [27] L. Zhang, Z. Q. Cao, T. Bai, L. Carr, J. R. Ella-Menye, C. Irvin, B. D. Ratner, S. Y. Jiang, *Nat. Biotechnol.* **2013**, *31*, 553.
- [28] L. R. Carr, H. Xue, S. Y. Jiang, *Biomaterials* **2011**, *32*, 961.
- [29] M. H. Li, J. H. Jang, B. X. Sun, Y. J. Surh, in *Signal Transduction Pathways, Chromatin Structure, and Gene Expression Mechanisms as Therapeutic Targets*, Vol. 1030 (Ed: M. Diederich), **2004**, p. 317.
- [30] Y. L. Lin, G. J. Li, *J. Mater. Chem. B* **2014**, *2*, 6878.
- [31] a) E. E. Totu, E. Ruse, R. Gardea, A. Grigorescu, *Optoelectron. Adv. Mater. – Rapid Commun.* **2008**, *2*, 442; b) Y. Zhang, S. L. Yuan, W. W. Zhou, J. J. Xu, Y. Li, *J. Nanosci. Nanotechnol.* **2007**, *7*, 2366.
- [32] Y. Y. Chen, H. Y. Lai, S. H. Lin, C. W. Cho, W. H. Chao, C. H. Liao, S. Tsang, Y. F. Chen, S. Y. Lin, *J. Neurosci. Methods* **2009**, *182*, 6.
- [33] a) M. Anderova, I. Vorisek, H. Pivonkova, J. Benesova, L. Vargova, M. Cicanic, A. Chvatal, E. Sykova, *J. Cerebral Blood Flow Metabolism* **2011**, *31*, 894; b) G. A. Lodygensky, T. West, M. D. Moravec, S. A. Back, K. Dikranian, D. M. Holtzman, J. J. Neil, *Magn. Reson. Med.* **2011**, *66*, 839.
- [34] T. Tourdias, N. Mori, I. Dragonu, N. Cassagno, C. Boiziau, J. Aousudre, B. Brochet, C. Moonen, K. G. Petry, V. Dousset, *J. Neuroinflammation* **2011**, *8*.
- [35] A. M. Fukuda, J. Badaut, *J. Neuroinflammation* **2012**, *9*.
- [36] J. N. Turner, W. Shain, D. H. Szarowski, M. Andersen, S. Martins, M. Isaacson, H. Craighead, *Exp. Neurol.* **1999**, *156*, 33.
- [37] M. R. Abidian, K. A. Ludwig, T. C. Marzullo, D. C. Martin, D. R. Kipke, *Adv. Mater.* **2009**, *21*, 3764.
- [38] T. D. Y. Kozai, X. Li, L. M. Bodily, E. M. Caparosa, G. A. Zenonos, D. L. Carlisle, R. M. Friedlander, X. T. Cui, *Biomaterials* **2014**, *35*, 9620.
- [39] P. Fattahi, G. Yang, G. Kim, M. R. Abidian, *Adv. Mater.* **2014**, *26*, 1846.
- [40] D. X. Tan, L. C. Manchester, R. Sainz, J. C. Mayo, F. L. Alvarez, R. J. Reiter, *Expert Opin. Ther. Patents* **2003**, *13*, 1513.